Chemical Engineering Journal 538 (2026) 176722

Contents lists available at ScienceDirect

Chemical Engineering Journal

journal homepage: www.elsevier.com/locate/cej

Multiphase interfacial transport engineering governs CO_2 availability in liquid-fed bicarbonate electrolysis

Ilias Stamatelos [a,*], Steffen Hess [b], Joachim Pasel [a], Ralf Peters [a,c]

[a] Institute of Electrochemical Process Engineering (IET-4), Forschungszentrum Jülich GmbH, 52425, Jülich, Germany
[b] Institute of Theory and Computation of Energy Materials (IET-3), Forschungszentrum Jülich GmbH, 52425, Jülich, Germany
[c] Ruhr University Bochum, Chair of Process Engineering for Synthetic Fuels, Bochum, Germany

ARTICLE INFO

Keywords:
Bicarbonate electrolysis
Multiphase transport
Membrane–electrode assembly
Interfacial morphology
CFD modeling
CO_2 utilization

ABSTRACT

Liquid-fed bicarbonate electrolysis offers a promising route for coupling carbon capture with electrochemical CO_2 conversion; however, performance under high-current operation is fundamentally constrained by the availability and transport of in situ–generated CO_2 at the membrane–electrode interface. In these systems, effective reactant delivery is governed by reaction–transport coupling and multiphase flow rather than bulk CO_2 concentration alone. Here, we demonstrate that regulating interfacial morphology and surface functionality enhances local CO_2 retention and phase distribution under convective conditions. Amine-functionalized catalyst layers modify interfacial acid–base conditions and improve CO_2 retention, while microstructured Nafion membranes stabilize localized gas-phase CO_2 holdup zones and mitigate interfacial depletion. Two-phase computational fluid dynamics simulations coupled with electrochemical measurements reveal a direct structure–transport–performance relationship, showing that enhanced superficial CO_2 mass fraction governs sustained activity. The integrated strategy enables selective CO production with Faradaic efficiencies of ~80% at 500 mA cm^{-2} and stable operation exceeding 160 h. These findings establish multiphase interfacial transport as a critical engineering parameter in bicarbonate electrolysis and provide design guidelines for scalable liquid-fed CO_2 conversion systems.

1. Introduction

Rising levels of atmospheric carbon dioxide (CO_2) have intensified research into sustainable mitigation strategies, with electrochemical CO_2 reduction (ECR) emerging as one of the most promising methods [1–3]. Over the past decade, significant progress has improved our understanding of ECR fundamentals and expanded its potential uses [4–8]. Depending on the catalyst used, ECR can produce a variety of value-added chemicals [9]. Among these products, carbon monoxide (CO) stands out as especially valuable as a key part of syngas, which serves as the feedstock for Fischer–Tropsch synthesis and other chemical upcycling processes [10].

Conventional CO_2 electrolyzers typically rely on high-purity gaseous feeds [11], where carbonate formation, CO_2 crossover, and downstream separation impose significant efficiency penalties and limit overall CO_2 utilization [12,13]. Direct (bi)carbonate electrolysis (DCE) has emerged as an attractive alternative, enabling integration of carbon capture and conversion within a single device by generating CO_2 in situ (i-CO_2) via the reaction of membrane-transported protons (H^+) with (bi)carbonate species [14–16]. Early demonstrations of this technology showed promising CO selectivity (FE_{CO}) of ~80% but at modest current densities (~100 mA cm^{-2}) [17,18]. The central limitation of direct bicarbonate electrolysis arises from how reactive CO_2 is supplied. Unlike gas-fed systems, CO_2 is generated in situ (i-CO_2) at the membrane–electrode interface through proton-mediated reactions with (bi)carbonate species. Under operating conditions, this CO_2 initially forms as a gaseous phase, and its retention and redistribution within the porous catalyst layer are critical for sustaining electrochemical reduction. As a result, local CO_2 availability at catalytic sites remains inherently limited, particularly at high current densities, due to constraints imposed by proton flux, bicarbonate–CO_2 equilibria, and transport within the electrode structure [19,20]. Although catalyst-layer microenvironment control, such as the incorporation of proton-conducting ionomers, can enhance local i-CO_2 generation near active sites [21], this does not address the dominant transport limitation. Under liquid-fed conditions, CO_2 availability is governed by interfacial transport at the membrane–electrode interface,

* Corresponding author.
E-mail addresses: i.stamatelos@fz-juelich.de (I. Stamatelos), s.hess@fz-juelich.de (S. Hess), j.pasel@fz-juelich.de (J. Pasel), ra.peters@fz-juelich.de (R. Peters).

https://doi.org/10.1016/j.cej.2026.176722
Received 12 February 2026; Received in revised form 24 April 2026; Accepted 25 April 2026
Available online 27 April 2026

including diffusion, convection, and gas–liquid phase exchange. Here, two-phase dynamics refer to the coexistence and transport of gaseous CO_2 and liquid electrolyte within the porous electrode, which can lead to spatial variations in gas holdup and local CO_2 concentration. Insufficient retention of gas-phase CO_2 can result in localized depletion of reactive CO_2 at the interface under convective flow. Consequently, catalytic performance is determined not only by intrinsic catalyst activity but also by the ability to sustain local CO_2 availability through controlled gas–liquid phase distribution and interfacial transport. Overcoming these constraints therefore requires strategies that couple chemical microenvironment control with interfacial transport engineering [22].

Tuning the physicochemical properties of electrocatalysts remains a powerful strategy for enhancing their reactivity [23], and surface functionalization with organic molecules has emerged as one of the most direct and effective approaches [24,25]. Among available strategies, the spontaneous grafting of diazonium salts—driven chemically or electrochemically—offers a versatile route for attaching a wide range of organic molecules, especially those containing primary amine groups ($–NH_2$), onto diverse electrode surfaces [26–29]. Amine functionalization has recently gained considerable attention because amines exhibit strong retention capacity for CO_2 and can modulate the local reaction environment of the catalyst layer [30,31]. For ECR systems, grafting amine-containing molecules can improve several key aspects of catalytic performance: (i) pre-binding CO_2, thereby increasing its local concentration near active sites and alleviating mass-transport limitations, [32,33] (ii) adjusting the local pH through their intrinsic alkalinity, which mitigates local acidification and suppresses the competing hydrogen evolution reaction (HER), [34] (iii) modulating the adsorption of the *CO intermediate, favoring the ECR over HER, [35] and (iv) tuning surface hydrophilicity, improving gas–electrolyte contact and reactant delivery [36,37]. Using this approach, Nazari et al. [38] demonstrated nearly a 6-fold increase in C_2^+ selectivity on Cu films, as a result of the supporting role of the molecular moieties to the ECR active catalyst centers. Amine functionalities, therefore, offer a practical route to modify interfacial CO_2 retention and local acid–base conditions without altering intrinsic catalyst composition.

Beyond adjusting the catalyst layer properties, performance limitations can also be overcome by engineering the morphology and spacing of the membrane–electrode assembly (MEA) interface. [39] Imprinting microstructures onto ion-exchange membranes has emerged as an effective strategy to enhance electrochemical performance [40]. Widely applied to Nafion-based membranes in well-known technologies, such as fuel cells, due to their chemical stability, this approach increases the effective membrane area and creates microchannels that improve reactant delivery and product removal [40–42]. These structures promote uniform mass transport and higher conversion efficiency [43]. Additionally, microstructured membranes are known to also improve water and ion management by maintaining local hydration, enhancing ionic conductivity, and facilitating the uniform distribution and rapid detachment of gas bubbles, thereby reducing mass-transfer limitations. Together, these effects yield higher performance and long-term stability, particularly under high current densities [44–46].

In this work, we demonstrate that overcoming CO_2 availability limitations in liquid-fed bicarbonate electrolysis requires simultaneous regulation of interfacial reaction chemistry and multiphase transport at the membrane–electrode interface. We implement a composite membrane–electrode assembly strategy in which amine-functionalized catalyst layers enhance CO_2 retention, while microstructured Nafion membranes regulate gas–liquid distribution and mitigate interfacial depletion under convective flow. Guided by two-phase computational fluid dynamics simulations and validated experimentally, this approach establishes a direct link between interfacial morphology, CO_2 mass-fraction distribution, and electrochemical performance. The engineered assemblies sustain selective CO production ($FE_{CO} \sim 80\%$ at 500 mA cm^{-2}) with stable operation up to 160 h. These findings highlight reaction–transport coupling as a governing factor in bicarbonate electrolysis and provide a framework for interfacial transport engineering in scalable liquid-fed CO_2 conversion systems.

2. Experimental procedures

2.1. Materials

We obtained demineralized water (MiliQ), carbon paper (Toray TGP-H-090), porous transport layers made from titanium fibers (Ti-PTL, with a thickness of 500 μm), Nafion dispersed in alcohol-based solution at a weight percentage of 5% wt/wt, Nafion 117 membrane, and carbon black (Cabot Vulcan XC-72) from the Fuel Cell Store. Additionally, we purchased a standard single-cell electrolyzer for CO_2 reduction applications from Dioxide Materials. Concentrated hydrochloric acid (HCl, 37% *w*/w), Iron powder (99.9% Fe, 100 μm), melamine (99.99%), potassium bicarbonate (98.9%), silver nano-particles (50 nm), silver foam (85% porosity), Iridium oxide nanoparticles (99.9%), ethanol (EtOH, anhydrous) & isopropanol (IPA, anhydrous), polyvinyl-4-pyrolidon (PV4P), sodium nitrite ($NaNO_2$ 99.99% anhydrous), sodium perchlorate ($NaClO_4$, 99.9% anhydrous) and cobalt phthalocyanine (CoPc, 99.9%) were bought from Sigma Aldrich.

2.2. Catalyst preparation

The different modified catalyst materials were fabricated using the melamine Grafting reaction, utilized in a wet-chemical or electrografting form.

2.2.1. Melamine-grafted nano-particles

The wet-chemical grafting of melamine over carbon black (CB) and silver (Ag) nanoparticles was conducted as previously reported by Grondein et al. [47]. An equimolar amount of nanoparticles and melamine was dispersed in water, along with an amount of $NaNO_2$ under the stoichiometric ratio of 2/3 of the melamine content. After rigorous stirring, the solution was brought to pH $\sim$ 2 after the addition of concentrated HCl. The grafting reaction was catalyzed by the addition of 160 mg Fe powder, and left to stir for 90 min. Afterwards, the dispersion was separated, and the powder was re-dispersed into an aqueous solution of 1 M HCl and sonicated for 30 min, for the leftover Fe to be dissolved. After separation, an additional cleaning step of sonication of MilliQ water was undergone. Finally, the powder underwent 1 washing cycle with KCl/water solution and 3 washing cycles with MilliQ water. The functionalized washed powders (CB/M and Ag/M) were left to dry overnight at 60 °C.

2.2.2. Melamine-grafted silver foam

The melamine functionalization of the silver foam (Ag_F) substrate was done via the Electro-Grafting reaction of melamine, as previously reported by Kesavan et al. [48] Briefly, a cleaned full-sized Ag_F substrate was immersed in the melamine-grafting solution (identical to that used for nanoparticle grafting but without Fe powder) inside an H-cell. In a three-electrode configuration, Ag_F served as the cathodic working electrode, and cyclic voltammetry (CV) was applied in the range of [−0.7 to +0.6 V] (vs. Ag/AgCl) to drive the electrochemical attachment of melamine molecules. The grafting process is a one-electron reaction ($n = 1$) occurring within the potential window of [−0.55 to −0.35 V] (vs. Ag/AgCl).To match the theoretical melamine loading obtained via wet-chemical grafting of Ag and CB nanoparticles, the number of CV cycles was adjusted assuming 100% reaction efficiency. Specifically, 105 cycles at a scan rate of 100 mV s^{-1} were applied. The charge (Q) consumed per cycle in the grafting potential window was determined by integration and, using Faraday's law, translated into the number of grafted melamine molecules. The total cycle count was then linearly scaled to achieve the target-grafted amount on Ag_F. After the end of the reaction, the functionalized substrate (Ag_F/M) was washed with copious amounts of MilliQ water and left to dry overnight at 60 °C.

2.3. Nafion membrane preparation

Oversized pieces of the Nafion 115 roll were activated as previously reported to assist in its transition to its protonated form [49]. The activated membrane was used later on for the electrochemical experiments in the single-cell.

For fabrication of the microstructured membrane, Nafion 117 was hot-pressed against a Ni foam template to imprint its surface morphology. The process was carried out at 130 °C (above the glass transition temperature of Nafion) and 0.2 kPa for 5 min, enabling partial softening of the membrane and conformal replication of the Ni foam structure. After cooling to room temperature, the membrane was mechanically detached from the Ni template and subsequently subjected to acid treatment to remove any residual metal. As a result, the Ni foam serves exclusively as a sacrificial structuring template and is not present in the membrane during electrochemical operation. Afterwards, the structured membrane pieces were soaked in a solution of HCl/H_2O_2 (1/1, M/M), and left overnight to dissolve leftover Ni traces. Following, the pieces were washed with copious amounts of MilliQ water and left to dry at RT for 48 h. After that, the micro-structured membranes were typically used for single-cell experiments, as intended.

2.4. Porous transport layers preparation

All porous transport layers (PTLs) used for the electrochemical experiments (i.e., silver foam, Toray carbon paper, titanium PTL) and for the membrane micro-structuring (i.e., nickel foam) were cleaned before use. The cleaning process involved sonication steps of 10 min duration, in the order of: MilliQ water, acetone, MilliQ water. Afterwards, the PTLs were dried overnight at 60 °C.

2.5. Electrode preparation

All catalyst-coated substrates were made using Toray carbon paper as a substrate and coating the catalyst dispersion by an automated spray-coating machine (Sono-Tek, ExactaCoat) over a vacuum-heating plate, at 70 °C. To make the CoPc ink, 156.44 mg of catalyst powder and 156.44 mg of melamine grafted carbon black were dispersed into a solution of PV4P in EtOH (1% wt./wt.) and 220 μl of Nafion solution (10% wt./wt.). The same ink recipe was applied for the case of silver nanoparticles grafted with melamine, where the total amount of solids of catalyst and catalyst support was replaced with the melamine grafted nanoparticles and dispersed into a solution of water/IPA (1/3) containing PV4P (1% wt./wt.). The catalyst inks were then subjected to Ultra-Turex at a speed of 33,000 rpm for 10 min before being placed in a sonication ice bath for sixty minutes. The cathode electrodes that contained the catalyst had a loading level of 2 mg cm^{-2}. For the anode of the MEA, a porous transport layer (PTL) made from Ti fiber mesh was used. The initial Ti-PTL was etched in boiling HCl (1 M), removing the outer passivating TiOx layer. The ink recipe for this layer included 160 mg of IrOx and 800 mg of Nafion ionomer dispersed in a 5% wt./wt. ethanolic solution, which was then mixed with 60 ml of methanol. This ink mixture was treated with Ultra-Turex at 33,000 rpm for 10 min, followed by sonication in an ice bath for one hour. The IrOx catalyst layer was spray-coated onto a Decal transfer sheet, maintaining a loading of 1 mg cm^{-2}, and then transferred by hot-pressing onto the membrane. The hot-pressing conditions were 150 °C under 1500 Bar for 10 min to ensure good contact and lamination of the IrOx layer with the membrane.

2.6. Electrochemical measurements

To evaluate the direct bicarbonate electrolysis, all experiments were conducted in a zero-gap MEA configuration with continuous catholyte recirculation, with an active area of 5 cm^2. The catholyte consisted of a 0.2 M $KHCO_3$ solution. The cathode was in direct contact with the Nafion membrane, while 0.2 M $KHCO_3$ was circulated through the cathode flow field, and water was circulated through the anode flow field. The use of 0.2 M $KHCO_3$ serves as a model system to isolate interfacial transport effects rather than replicate industrial capture conditions. The anode consisted of IrOx/Ti–PTL, and the anolyte was MilliQ water. An activated Nafion PEM (117) membrane was employed for the standard electrochemical experiments, which was later on microstructured, for the enhancement of the i-CO_2 availability. Both the anolyte and catholyte were continuously recirculated throughout electrolysis, with a pumping rate of 50 ml min^{-1}, from their respective gas-tight closed tanks of 250 ml volume. The catholyte tank was purged with CO_2 (30 sccm) for standard testing and purged with N_2 (30 sccm) for investigation purposes. Under CO_2 purging, the electrolyte remains in equilibrium with CO_2, stabilizing the carbonate/bicarbonate system and mitigating alkalinity drift during operation. During the initial performance screening (polarization curve and product selectivity measurements), the catholyte was refreshed after the end of each full measurement of each sample. During stability measurements, the catholyte was refreshed every 4–8 h. The used PTFE gaskets had a total thickness of 400 μm, and the assembly of the cell involved applying three Nm torque to each screw of the electrolyzer. The MEA cell was held together by four screws. In both cases, catalyst-loaded cathode PTLs served as cathode materials and were placed facing the cathodic side of the PEM membrane during assembly, which was later the microstructured one. All measurements in the zero-gap single cell, were conducted at a constant compression of 5%, using the standard thickness PTFE gaskets as cell compression modulators. The loading of the cathodic catalyst side was fixed at 2.2 mg cm^{-2} in between the PTL-PEM MEA interface. The anodic IrOx CCM side of the PEM where placed facing the anode, and on top the anodic Ti-PTL was placed. To generate a polarization curve, the cell was operated continuously at a fixed current for 25 min. Throughout this period, the voltage (on average) required to maintain this current was measured, and the gas products were sampled after 20 min. The different electrochemical experiments were conducted using an AUTOLAB potentiostat coupled with a 20 A booster, supported by Nova software as a means of control. All the potential reported potentials are without iR correction.

To examine the CO_2 reduction products in the flow cell and MEA reactors, we utilized inline gas chromatography from Agilent. This analysis employed a thermal conductivity detector (TCD) and a flame ionization detector (FID). Argon (99.999%) was used as the carrier gas. The measurement of the gas flow rate at different points along the polarization curve was conducted at the gas outlet of the cell. All of these experiments were carried out at room temperature (RT).

2.7. Electrochemical characterizations

PEIS measurements were conducted at the onset potential and at 200 mA cm^{-2} of each Electrode within a frequency range of 10^5–$4\bullet10^{-2}$ Hz, into the single-cell. To assess the electrochemical surface area (ECSA), the double-layer capacitance (C_{dl}) was calculated for each electrode, both in an H-cell and in the single-cell. By directly comparing C_{dl} values, trends in ECSA could be observed among different electrodes loaded with various catalysts. The experiments took place in an H-cell using an Ag/AgCl reference electrode and a Pt wire as a counter-electrode. A standard electrolyte solution containing 0.1 M $NaClO_4$ was used, which had been saturated with argon gas. In the single-cell, the C_{dl} measurements were used to assess the influence of the micro-structured membrane on the MEA surface area. Cyclic voltammetry scans were conducted at scan rates ranging from 20 to 100 mV sec^{-1}. Current density measurements were obtained from the non-faradaic region of the cyclic voltammograms.

2.8. Characterization of the catalyst materials

To analyze the surface composition and states of the catalysts, X-ray

photoelectron spectroscopy (XPS) was employed. The instrument used for this analysis was the Phi5000 VersaProbeII by ULVAC-Phi Inc., USA, utilizing Al K-alpha radiation at a monochromatic energy of 1.486 keV. The X-ray settings were as follows: 50 W power, 15 kV voltage, and a spot size of 200 μm. For obtaining survey spectra, a pass energy of 187.5 eV with an increment step size of 0.8 eV and an acquisition time per step set to be at 100 ms/step was applied; whereas for detailed spectra acquisition pass energy was changed to 23.5 eV with an increment step size reduced to only 0.1 eV while keeping the time per step constant at 100 ms.

Raman and FT-IR spectroscopy provided additional information regarding the successful grafting and chemical species on the functionalized materials. The Raman experiments were carried out in a confocal Raman microscope (Renishaw) in backscattering geometry. This system was equipped with a frequency-doubled Nd-YAG laser (wavelength: 532 nm) and a CCD detector. The backscattered signal was collected through a 100× objective lens (working distance ~300 μm) and dispersed by a 2400 grooves per mm grating. The laser power density was kept below 0.5 mW/μm^2 to avoid heating effects and thermal damage of the investigated materials. To observe the morphology of both catalyst powders and GDEs, a scanning electron microscope (SEM) was employed. Specifically, the Zeiss 1550 VP SEM with a Gemini column was utilized at voltages up to 30 keV. TEM and HRTEM measurements were conducted using a Philips CM 200 field emission gun with an accelerating voltage set at 200 kV. To achieve optimal "*Z*-contrast" conditions, a probe semi-angle of 25 mrad was employed alongside an inner collection angle of 70 mrad by the detector. The surface characteristics of the microstructured membrane.

The hydrophobicity of the catalyst layer was measured with a Kruss DSA25 Drop Shape Analyzer. Ten μL of Milli-Q water was automatically dropped on the GDE's catalyst layer for each measurement. Under static conditions (Cassie–Baxter), the value of the contact angle is measured. The nitrogen (N_2) adsorption–desorption isotherm and the specific surface area (SSA) values calculated according to the Brunauer–Emmett–Teller (BET) method were obtained at −196 °C with a Micromeritics ASAP-2020 system. The CO_2 adsorption of the functionalized samples was measured in the same way, using CO_2 instead of N_2, and the measurement was conducted at RT. Before analysis, the samples were thermally treated (degassed) at 80 °C under a vacuum.

2.9. CFD model, methodology

The presented model of the CO_2 electrolyzer is part of an electrochemical cell model implemented in OpenFOAM®. This model exclusively focuses on the isothermal two-phase flow phenomena occurring on the anode side of the CO_2 electrolyzer, where gaseous, in situ generated CO_2 (i-CO_2) is generated via chemical reactions. Consequently, any changes in temperature, electrical potentials, or reaction kinetics are neglected in the present model.

The CFD model captures the multiphase transport processes, including the multicomponent transport of species in both the gas and liquid phases, as well as transport within the functional porous layers, based on an Eulerian–Eulerian two-phase flow approach. Specifically, it accounts for the phase change between dissolved CO_2 in the liquid electrolyte and gaseous CO_2 bubbles. The CFD model is intentionally formulated as a transport-focused model and does not explicitly resolve electrochemical reactions, ion transport, acid–base equilibria, or local pH evolution. In particular, OH^- generation at the cathode, proton transport through the membrane, and transport competition between K^+ and H^+ are not treated explicitly. Instead, in situ CO_2 generation is represented by an effective source term at the membrane interface derived from the applied Faradaic current density. This approach enables isolation of the influence of interfacial morphology on multiphase CO_2 transport, gas holdup, and local CO_2 distribution under otherwise identical operating conditions. With the assumptions used: (i) Newtonian fluids, (ii) laminar flow regime, (iii) no electrochemical reactions considered, (iv) CO_2 generation modeled as a dissolved species in the electrolyte based on the Faradaic current density, (v) CO_2 forms spherical bubbles, (vi) CO_2 generation occurs only at the membrane surface, with the rate defined by a constant Faradaic current density.

3. Results and discussion

3.1. Synthesis & characterization of the melamine grafted materials

Using a facile chemical synthesis approach, we successfully grafted melamine molecules onto carbon black (CB), silver (Ag) nanopowder, and silver foam (Ag_F). For CB and Ag-NP, such an approach has been previously demonstrated for various aryl diazonium salts, enabling the covalent attachment of aryl groups to various surfaces. [50,51] The grafting reaction was carried out via a wet-chemical route catalyzed by iron (Fe) powder (Fig. S1a), [52] while for Ag_F the process was electrochemically induced (Fig.S1b) [53]. The resulting melamine-functionalized materials—CB/M (as a catalyst substrate), Ag/M, and Ag_F/M—were employed as primary catalysts for CO_2-to-CO conversion.

Scanning Electron Microscopy (SEM) coupled with Energy-Dispersive X-ray Spectroscopy (EDX) was used to examine the morphology and elemental composition of the functionalized materials (Fig. 1a–c). The CB and Ag-NPs displayed average particle diameters of ~20 nm and ~ 50 nm, respectively, both before [54] (Fig. S2a) and after (Fig. 1a,b) the wet-chemical grafting process, indicating that the reaction did not alter the nanoparticle morphology. Likewise, the Ag_F surface exhibited no detectable morphological changes after the electrochemically induced grafting procedure (Fig. 1c & Fig. S2b). EDX elemental mapping confirmed the presence of nitrogen and carbon species on the functionalized surfaces, providing direct evidence of successful melamine attachment. As previously discussed, amine groups show increased interfacial interaction capacity under equilibrium conditions with CO_2 molecules, a property we aimed to utilize in catalysis. Besides their tailored surface chemistry, the functionalized materials were evaluated for their CO_2 adsorption capacity (Fig. S4d–f) and compared with their pristine counterparts. Adsorption data were normalized to each sample's specific surface area, determined by BET analysis (Fig. S4a–c), which remained constant for each material before and after its functionalization. CO_2 adsorption measurements (BET) at (Fig. 1d) indicate an increased CO_2 uptake capacity for the amine-functionalized surfaces, consistent with enhanced interfacial CO_2 retention. At 730 Torr of CO_2, grafting with melamine increased CO_2 uptake by approximately 37% for the nanoparticle-based materials (CB and Ag) and by about 25% for Ag_F. This increase highlights the role of grafted melamine layers in boosting surface CO_2 retention capacity. The greater adsorption seen in the nanoparticles (CB/M and Ag/M) compared to Ag_F is due to their larger specific surface area (Fig. S4a–d), which provides more accessible binding sites for CO_2. Overall, in aqueous electrochemical environments, CO_2–amine interactions are dynamic and can involve reversible physical interactions and bicarbonate formation rather than stable carbamate species. Under operating conditions, continuous electrochemical turnover and local pH gradients favor rapid CO_2 exchange, enabling sustained availability of electrochemically active CO_2(aq). The role of amine functionalities is therefore interpreted in terms of transient CO_2 retention and interfacial buffering rather than static chemical binding [55].

Fourier-transform infrared spectroscopy (FT-IR) and Raman spectroscopy (Fig. 1e,f) were also used to probe the surface chemical composition. The FT-IR spectra (Fig. 1e) revealed a broad absorption band at ~3000 cm^{-1}, corresponding to primary amine (–NH_2) stretching vibrations [56,57]. However, strong background contributions from the carbon and silver substrates masked weaker melamine vibrational features, making only the most abundant –NH_2 groups distinctly detectable [58,59]. In contrast, Raman spectra (Fig. 1f) provided complementary information: in addition to the –NH_2 vibrations, a distinct C—N

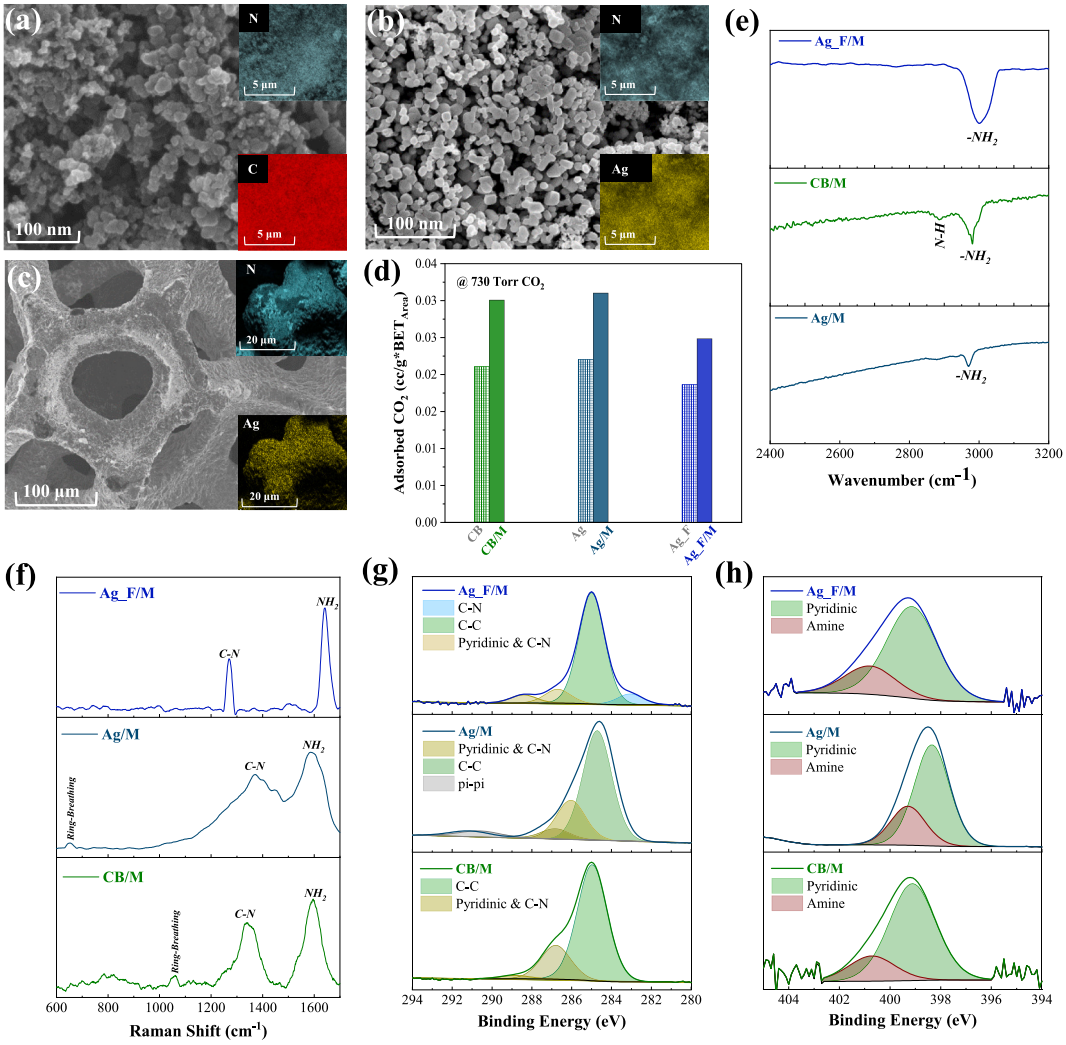

Fig. 1. Physico-chemical characterizations of the melamine-grafted catalyst materials. (a) SEM/EDX images of the melamine-grafted carbon black nano-particles (CB/M); (b) SEM/EDX images of the melamine-grafted silver nano-particles (Ag/M); (c) SEM/EDX images of the melamine-grafted silver foam (Ag_F/M); (d) BET normalized CO_2 adsorption of the different melamine grafted materials; (e) FT-IR spectra of the grafted materials; (f) Raman spectra of the grafted materials; (g) High-Resolution C-XPS of the grafted materials; (h) High-Resolution N-XPS of the grafted materials.

stretching mode at ~1350 cm^{-1} was observed, confirming the presence of a melamine-derived shell covalently bound to the substrates [27,60]. The differences in peak shape between the samples arise primarily from variations in spectral background and support material. Carbon-supported systems (carbon black) exhibit broad Raman features and elevated baselines due to structural disorder in sp^2 carbon and associated fluorescence contributions, which can lead to peak broadening and reduced resolution [61]. In contrast, Ag-based substrates provide a cleaner spectral background and improved signal-to-noise ratio, resulting in sharper and more well-defined vibrational features. This effect is further enhanced by the absence of carbon-related background contributions and the favorable optical properties of metallic surfaces [62,63].

The high-resolution X-ray photoelectron spectroscopy (XPS) of C 1 s and N 1 s (Fig. 1g,h) further validated these findings. Overall, the surface characterization techniques display characteristic bonding environments consistent with C—N and –NH_2 groups, directly attributable to melamine, and absent in the pristine control samples (Fig. S3a–e) [64]. The grafted melamine layer formed a film of ~10 nm around the nanoparticles and ~ 13 nm on the Ag_F surface (Fig. S4g). Although both the wet-chemical and electrochemical grafting routes resulted in comparable amounts of melamine bound to the surface (Fig. S3a), the observed thickness difference is attributed to the distinct specific surface areas of the nanoparticles (CB and Ag) versus the silver foam (Ag_F). Collectively, SEM/EDX, FT-IR, Raman, and XPS analyses provide consistent evidence for the successful covalent grafting of melamine molecules onto CB, Ag-NPs, and Ag_F surfaces.

3.2. *Electrochemical performance of the functionalized materials*

The electrochemical performance of the functionalized materials was evaluated in a zero-gap single-cell electrolyzer using a standard potassium bicarbonate solution as the standard electrolyte [34,65]. The use of 0.2 M $KHCO_3$ serves as a model system to isolate interfacial transport and phase behavior without additional effects from increased ionic strength, viscosity, and salt accumulation at higher concentrations. It should be noted that the use of 0.2 M $KHCO_3$ represents a model system to isolate interfacial transport and phase behavior, rather than replicate industrial bicarbonate concentrations (e.g., ~3 M). Under CO_2 purging, the electrolyte remains buffered, preventing significant alkalinity drift during long-term operation. This allows stable operation while enabling clear identification of transport-controlled limitations. The use of dilute electrolyte therefore enables isolation of interfacial transport effects, which are otherwise convoluted at higher bicarbonate concentrations [22]. Silver nanoparticles (Ag NPs) and silver foam (Ag_F), both established ECR catalysts for CO formation, were tested in their functionalized forms: Ag/M, incorporated into the catalyst layer and deposited on

carbon paper, and Ag_F/M, directly employed as electrodes [22,66]. These comparisons enabled assessment of melamine grafting on the direct bicarbonate electrolysis (DCE) performance. In parallel, carbon black (CB)—which is not intrinsically ECR-active and typically functions as a support—was functionalized (CB/M) and combined with cobalt phthalocyanine (CoPc), a molecular catalyst with well-documented activity and selectivity toward CO [67]. The optimal CoPc-to-CB/M ratio in the catalyst layer was determined to be 1:1 (CoPc_CB/M) (Fig. S5).

To evaluate electrode performance under industrially relevant conditions, we screened their activity across increasing current densities (j) until the Faradaic efficiency for CO (FE_{CO}) decreased to 70% [68]. The CoPc_CB/M and Ag/M electrodes demonstrated the most promising behavior, maintaining FE_{CO} values above 80% up to ~350 mA cm^{-2} (Fig. 2a,b). Both reached comparable maximum current densities, with CoPc_CB/M achieving 550 mA cm^{-2} (Fig. 2a) and Ag/M 600 mA cm^{-2} (Fig. 2b). In contrast, Ag_F/M was limited to ~400 mA cm^{-2}, likely due to its lower available surface area (Fig. S6b). Overall, the melamine-grafted materials exhibited much higher ECR activity in comparison to their original state (Fig. S5e-g). Standard electrode properties, including surface hydrophobicity (Fig. S6a) and electrochemically active surface area (ECSA) (Fig. S6b), remained essentially unchanged between pristine and functionalized samples, indicating that the enhanced performance of the functionalized electrodes (Fig. 2a–c) is attributed to the modified interfacial CO_2 retention and transport characteristics induced by melamine grafting. The polarization curves materials (Fig. 2d), in terms of CO partial current density (j_{CO}), reveal the onset of mass-transport limitations at high current densities (j_{CO} > 300 mA cm^{-2}), which we attribute primarily to the generation and local availability of in situ CO_2 at the membrane/catalyst interface, rather than to bulk ion transport or electrode properties [69]. At such rates, the critical rate-limiting step is the sufficient production and retention of interfacial i-CO_2, over the membrane/electrode interface [70]. These results indicate that the catalytic performance is governed by the local availability of $CO_{2(aq)}$, which is controlled by gas–liquid equilibrium, in situ CO_2 generation, and interfacial transport processes.

While catalyst-layer ionomer strategies can enhance local i-CO_2 generation near active sites, sustaining high-rate operation in liquid-fed MEAs additionally requires controlling the two-phase i-CO_2 local chemical environment and interfacial depletion under convective flow. To understand this device-level mass-transport bottleneck, we analyzed the generation and spatial distribution of in situ CO_2 at the membrane–electrode interface, where interfacial morphology critically governs reactant availability for ECR. Two-phase computational fluid dynamics (CFD) simulations were therefore employed to resolve phase-specific CO_2 mass fractions, and a local superficial i-CO_2 mass fraction—accounting for both dissolved and gaseous CO_2—was evaluated across different MEA architectures (Fig. S15). The model quantifies how interfacial geometry alters local gas holdup and effective diffusive transport toward the catalyst layer under steady-state convective conditions. It should be noted that the CFD model is used here to isolate the transport consequences of interfacial geometry rather than to reproduce the full electrochemical system. Thus, the simulations are interpreted comparatively, with both membrane geometries evaluated under the same effective CO_2 generation condition.

For a conventional flat membrane, simulations show that electrolyte convection induces uneven i-CO_2 distributions and localized depletion at the membrane–electrode interface, thereby limiting reactant availability. In contrast, imprinting microstructures [44] onto the Nafion membrane (Fig. S14) fundamentally alters the interfacial CO_2 distribution, yielding a markedly higher superficial i-CO_2 mass fraction within the valley regions (Fig. 2e). The simulations reveal spatial gradients in CO_2 mass fraction and gas holdup that directly influence effective reactant transport to the interfacial environment under convective flow. These results establish a direct structure–transport–function relationship, linking interfacial morphology to effective interfacial CO_2 transport. This enhancement stems from the preferential accumulation of gaseous CO_2 bubbles in the valleys, which increases local gas holdup and elevates the gas-phase CO_2 fraction (Fig. S15). As a result, the microstructured architecture mitigates interfacial i-CO_2 depletion and promotes more uniform reactant availability across the MEA. Importantly, the ~1.5–2 increase in valley-region i-CO_2 holdup relative to flat membranes (Fig. S15) directly correlates with proportionally higher sustained j_{CO} under identical operating conditions (Fig. 2d,f). Although electrochemical kinetics are not explicitly resolved, these results establish a clear structure–transport–performance relationship, identifying stabilized gas-phase i-CO_2 reservoirs at the membrane–electrode interface as a key design parameter for high-rate liquid-fed electrolysis.

3.3. Electrochemical performance under the effect of the microstructured membrane

For proof of concept, we have created such a micro-structured membrane to experimentally validate its effect during electrolysis. Our facile approach involved the gentle hot-pressing of Ni-foam to a common Nafion membrane (Fig. 2f), over the Nafion glass-transition point (T_g). This resulted in a fine-tuned micro-structured surface (Fig. S8&9).

The functionalized electrodes (CoPc_CB/M, Ag/M, Ag_F/M) were evaluated in a zero-gap electrolyzer using a microstructured Nafion membrane (Fig. 3a,b) instead of a planar one, yielding the samples CoPc_CB/M_P, Ag/M_P, and Ag_F/M_P. The effect of the microstructured membrane was primarily reflected in the increased electrochemical surface area (ECSA, Fig. S6c), determined from capacitance measurements. This improvement was further confirmed by electrochemical impedance spectroscopy (EIS). The Nyquist plots (Fig. S6d–f) revealed a lower charge transfer resistance (R_{ct}) and a higher time constant (τ), consistent with an enlarged membrane/electrolyte interface that enhances H^+ flux and increases MEA capacitance, respectively [41]. An effect directly correlated with the increase in cell voltage observed for all the MEA using a structured membrane (Fig. 3f) in comparison with the voltages of the plain-membrane MEAs (Fig. 2d). With the effect of the increased R_{ct} at the higher current densities range. As all experiments were performed under identical compression (5%), the observed differences arise from morphology-dependent effects rather than variations in applied mechanical pressure.

Using the same testing protocol as before, we then evaluated the CO selectivity of the modified MEAs across a wide range of current densities. The CoPc_CB/M and Ag/M electrodes again delivered the highest ECR activity, largely attributable to their high initial ECSA (Fig. S6b). The CoPc_CB/M_P MEA (Fig. 3c) maintained a CO Faradaic efficiency (FE_{CO}) of around 80% up to ~400 mA cm^{-2} and remained above 70% up to 700 mA cm^{-2}. The Ag/M_P MEA (Fig. 3d) sustained high selectivity, with FE_{CO} values near 80% up to 500 mA cm^{-2} and still above 70% at 800 mA cm^{-2}. The Ag_F/M_P MEA (Fig. 3e) also exhibited enhanced performance, achieving FE_{CO} of ~80% up to 350 mA cm^{-2} and maintaining ~70% at 500 mA cm^{-2}. Overall, comparison of the polarization curves (Fig. 3f) confirmed that the Ag/M_P MEA delivered the highest performance, reaching a maximum j_{CO} of 550 mA cm^{-2} and demonstrating ampere-level electrolysis.

The increased interfacial area of the microstructured MEA promotes more uniform retention and distribution of in situ–generated CO_2 (i-CO_2), ensuring a steady reactant supply to the catalyst layer under high-current operation (Fig. 3f). The wavy membrane architecture provides a substantially larger effective surface area (Fig. 3a,b, Tables S3–S5), which not only improves spatial distribution but also enhances i-CO_2 retention at the reaction front under convective electrolyte flow (Fig. S15). Within the cavern-like features of the membrane, CO_2 generated near the membrane–electrolyte interface initially dissolves in the liquid phase and accumulates locally. When the dissolved CO_2 concentration exceeds its solubility limit, gas nucleation occurs, leading to CO_2 bubble formation. These bubbles preferentially reside in the valleys of the wavy structure and subsequently migrate toward the catalyst layer. The resulting localized gas-phase CO_2 holdup zones that enhance

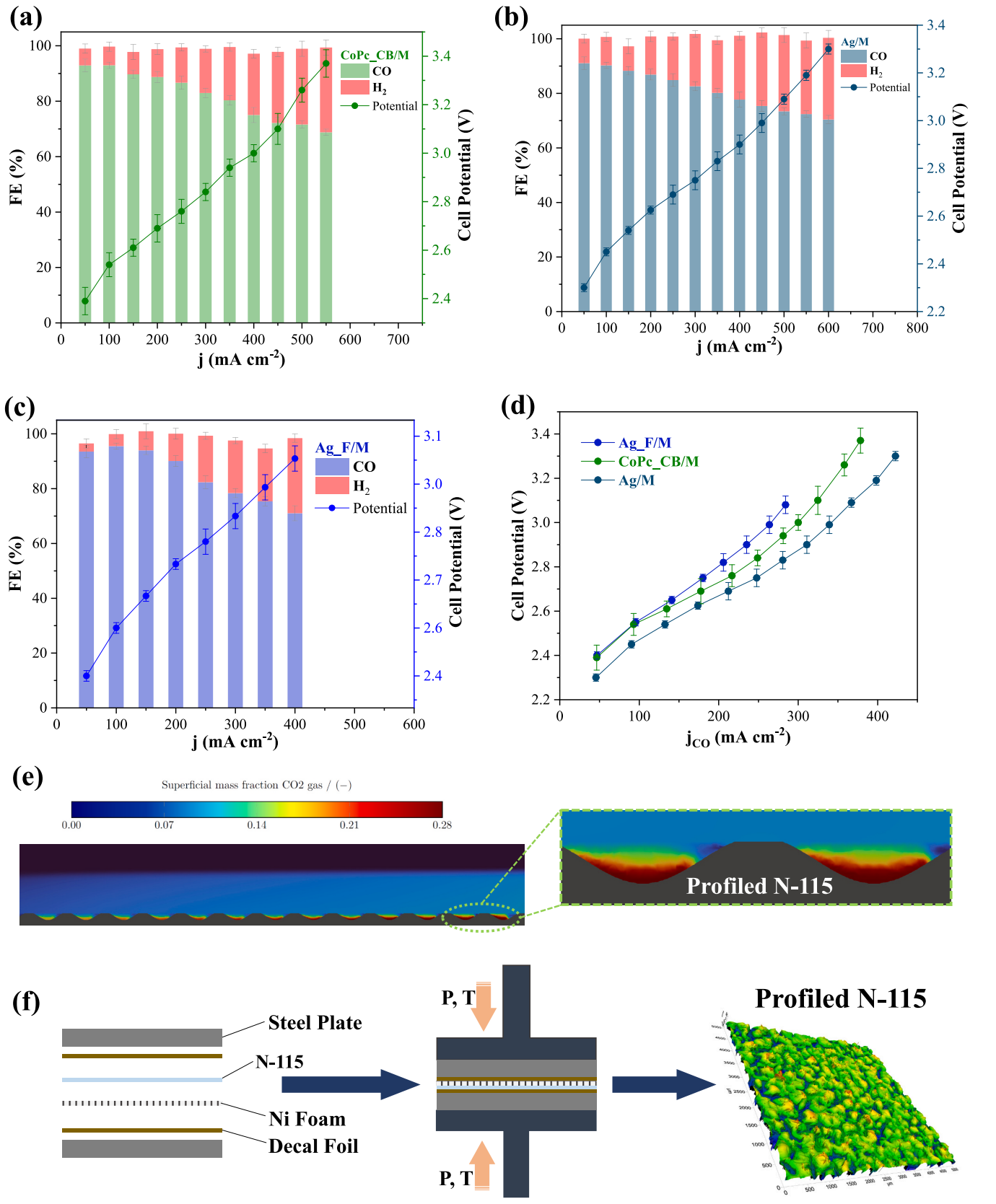

Fig. 2. Electrochemical performance of the different melamine-grafted catalyst materials and membrane characteristics. (a) Performance of the melamine grafted carbon black (CB/M) nanoparticles, using a CoPc catalyst (CoPc_CB/M); (b) Performance of the melamine-grafted silver nano-nanoparticles (Ag/M); (c) Performance of the melamine-grafted silver foam (Ag_F/M); (d) Polarization curve, in terms of partial current density for CO (j_{CO}), of the different materials; (e) Computational Fluid Dynamics (CFD) simulation of i-CO_2 concentration distribution over the microstructured membrane; (f) Graphical representation of the microstructured-membrane fabrication process.

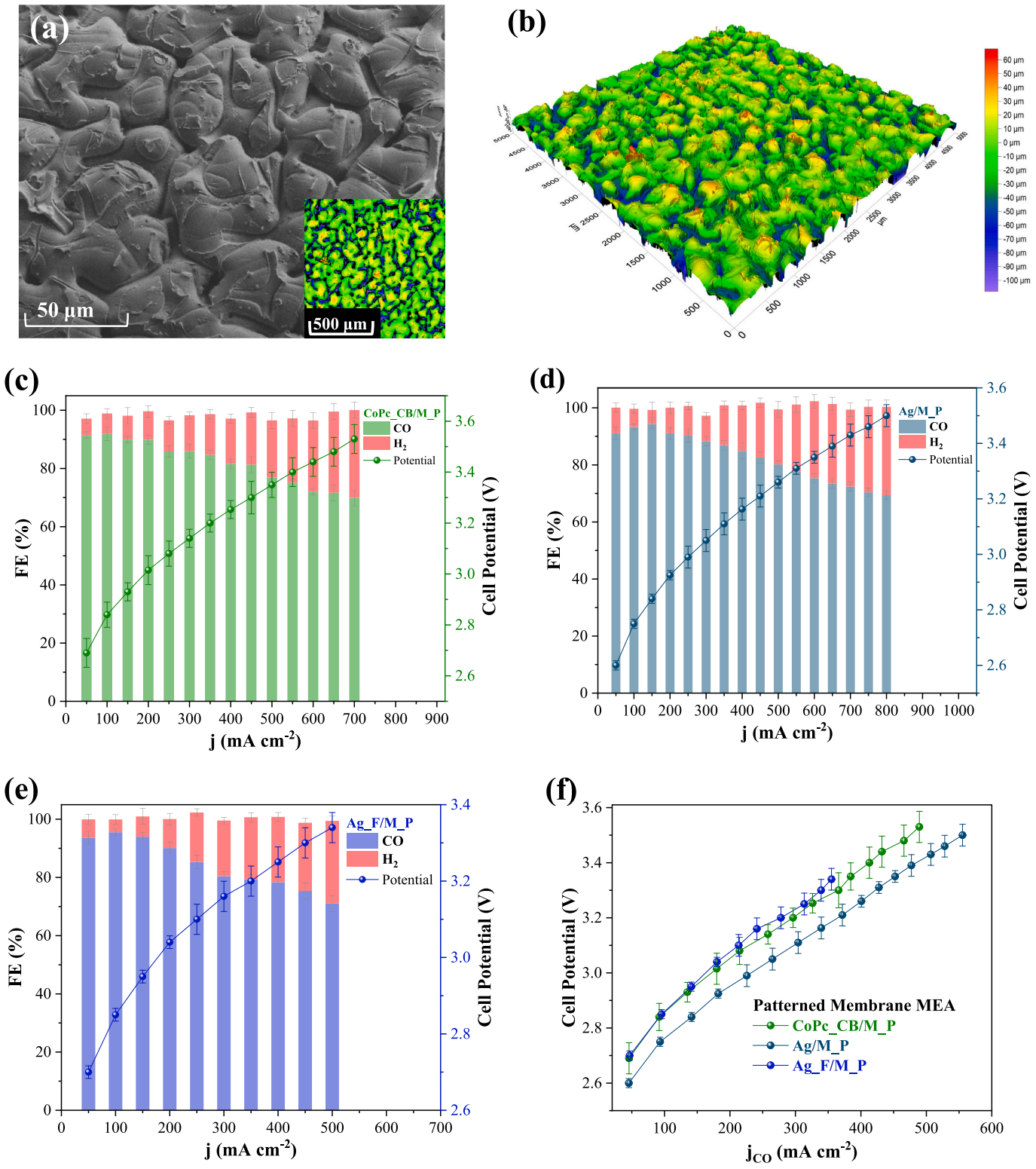

Fig. 3. Characterization of the microstructured membrane and evaluation of its influence on the ECR performance. (a) SEM and 2-D laser scanning imaging of the microstructured membrane's surface; (b) Detailed 3-D imaging of the microstructured membrane, using laser scanning; (c) Performance of the melamine-grafted carbon black nanoparticles, with a CoPc catalyst, using the microstructured-membrane (CoPc_CB/M_P); (d) Performance of the melamine-grafted silver nano-nanoparticles, using the microstructured membrane (Ag/M_P); (e) Performance of the melamine-grafted silver foam, using the microstructured membrane (Ag_F/M_P); (f) Polarization curve, in terms of partial current density for CO (j_{CO}), of the different materials, using the microstructured membrane.

diffusive transport toward the catalyst layer near the catalyst–membrane interface, enabled by the microstructured geometry, is therefore proposed to contribute to the enhanced electrolysis performance by improving multiphase CO_2 distribution and reactant flux. This effect is consistent with the higher diffusivity of gaseous CO_2 compared to dissolved CO_2 in aqueous electrolytes (Table S2), which facilitates more efficient reactant transport to the catalyst surface and alleviates mass-transport limitations.

To clarify the origin of electrochemically active CO_2, control experiments were conducted under continuous N_2 purging conditions (Fig. S12 a&b), thereby minimizing the contribution of externally dissolved CO_2, while preserving bicarbonate-derived CO_2 generation, confirming that the observed activity is not solely due to externally dissolved CO_2. Under these conditions, measurable CO formation is still observed, confirming that bicarbonate-derived in situ CO_2 contributes directly to the electrochemical reaction. As expected, the absolute current densities are lower compared to CO_2-purged operation, indicating that dissolved CO_2 can contribute to the overall CO_2 supply. Importantly, however, the relative performance trends between electrode and membrane configurations are preserved. This demonstrates that the observed performance enhancement is governed by interfacial CO_2 retention and transport phenomena rather than the absolute CO_2 source. Accordingly, the conclusions of this work reflect transport-controlled CO_2 availability at the membrane–electrode interface. We note that electrochemical reduction proceeds via dissolved $CO_{2(aq)}$, while the in situ generated gas-phase CO_2 acts as a reservoir that maintains local CO_2 concentration and availability through dissolution. Therefore, the conclusions of this work reflect transport-controlled CO_2 availability at the membrane–electrode interface.

3.4. Long-term stability of the electrolysis system

Building on the promising performance of our functionalized catalysts and the novel MEA architecture (Fig. 3), we next evaluated the stability of the electrolysis systems under constant operating conditions. The objective was to exploit the enhanced i-CO_2 flux provided by the microstructured membrane to sustain high reaction rates, using the functionalized Ag/M electrode as the model system. These stability experiments were designed to identify potential degradation mechanisms responsible for the loss of ECR selectivity. Among the developed

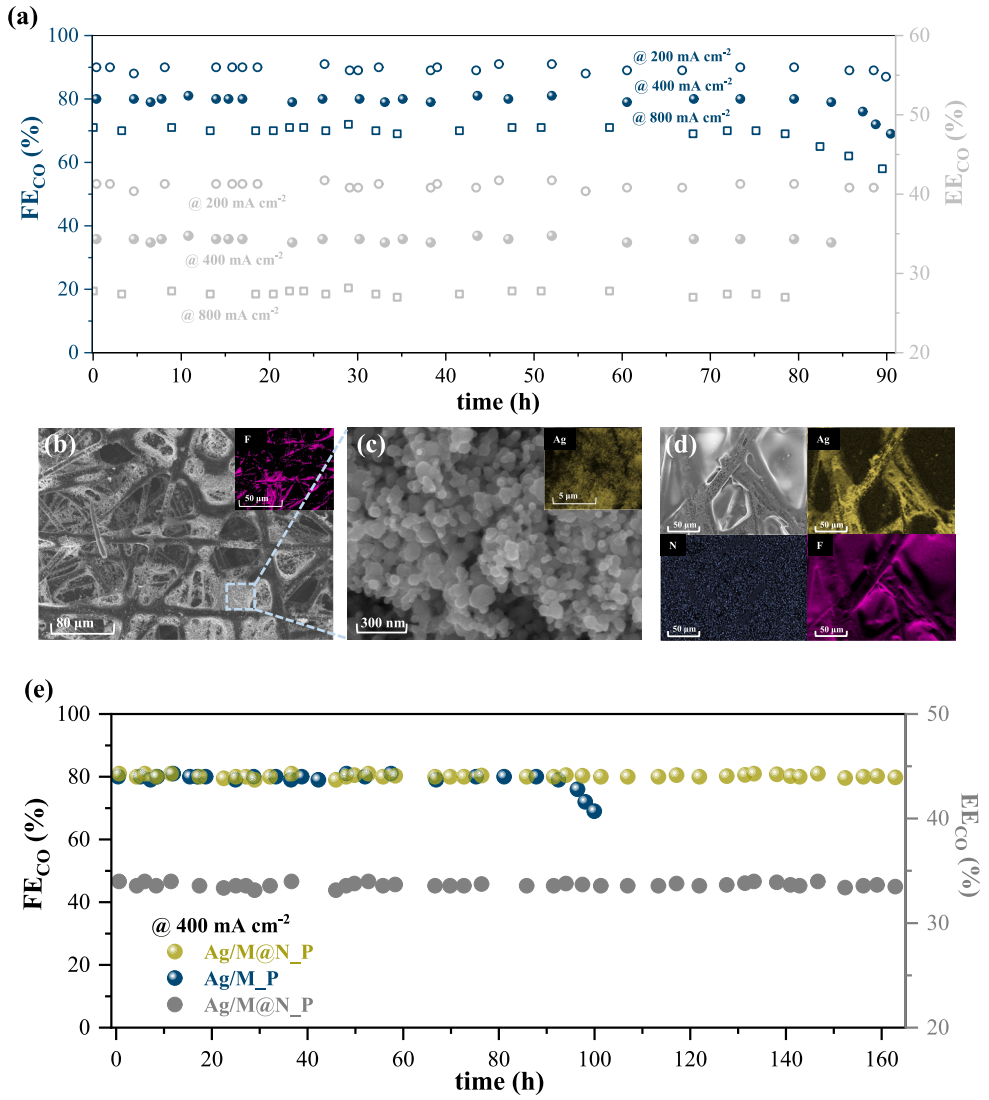

Fig. 4. Evaluation of the ECR stability of the melamine grafted silver nanoparticles electrode, using the microstructured membrane MEA. (a) ECR stability and energy efficiency for CO (EE_{CO}) at different current densities; (b) SEM/EDX post-mortem characterization of the Ag/M electrode, after 80 h of constant electrolysis at 400 mA cm^{-2}; (c) High-magnification SEM/EDX post-mortem characterization of the electrode after 80 h of electrolysis at 400 mA cm^{-2}; (d) SEM/EDX characterization of the melamine grafted silver nano-particles electrode spray-coated with an additional Nafion overlayer (Ag/M@N_P); (e) ECR stability and energy efficiency for CO (EE_{CO}) at 400 mA cm^{-2} of the Ag/M@N and Ag/M electrodes, using the microstructured membrane.

materials, we focused on the silver-based catalysts—primarily the Ag/M electrode—given the inherent stability of silver nanoparticles and substrates under ECR conditions [71,72]. This allowed us to isolate and examine the influence of other factors, such as melamine functionalization and MEA architecture, on long-term performance deterioration.

Given the previously demonstrated high performance of the Ag/M_P MEA (Fig. 3d), its stability was evaluated under current densities ranging from 200 to 800 mA cm^{-2} with a constant catalyst loading of 2 mg cm^{-2} (Fig. 4a). Across these conditions, the MEA exhibited declining CO selectivity (FE_{CO}) and energy efficiency (EE_{CO}) with increasing current density, primarily due to the higher cell voltage required to sustain elevated reaction rates. Despite this, operational stability was consistently ~80 h across all current densities, suggesting that performance loss was not dominated by depletion of electrochemical reduction (ECR) active sites, as stability appeared independent of the reaction rate [73].

To investigate the source of degradation, post-mortem SEM/EDX analysis was conducted on the Ag/M electrode (Fig. 4b,c). The results showed minimal detachment of the silver-based catalyst layer and no significant change in nanoparticle dimensions, confirming the morphological stability of the catalyst and the preservation of its active sites under electrolysis conditions. However, the EDX spectra showed no N-species on the catalyst surface, suggesting that melamine functionalities were washed away during extended electrolysis. The observed performance decay is attributed to the loss or degradation of melamine-derived surface functionalities under operating conditions. To confirm this mechanism, the Ag_F/M electrode was subjected to extended electrolysis at a similarly high current density (Fig. S10a). After 80 h, SEM/EDX analysis again showed maintained silver morphology (Fig. S10b,c), but no detectable N-species on the surface (Fig. S10d). Complementary EDX line scans (Fig. S11b,c) confirmed the progressive diminishment of the nitrogen signal across the scanned regions, strongly indicating that the loss of melamine functionalities—rather than catalyst degradation—was the limiting factor for long-term electrolysis performance. The stability of the microstructured membrane under relevant conditions was confirmed by SEM and laser scanning across different processing stages. The patterned membrane retains its imprinted features both before (Fig. S8a) and after prolonged wet-chemical treatment (Fig. 3a&b). Post-mortem SEM analysis after long-term electrolysis (Fig. S8e) further shows that the microstructured morphology remains clearly preserved, with only minimal swelling observed. These results demonstrate that the membrane structure is robust under hydrated and operating conditions, confirming that the observed transport effects are not artifacts of dry-state morphology.

These findings suggest that extended electrolysis operation could be realized if the grafted melamine moieties were retained on the catalyst layer for longer durations. To postpone their detachment and enhance stability, we applied an additional ionomer overlayer on the Ag/M catalyst surface. Such Nafion-overlayers are frequently employed in electrolysis technologies to mitigate catalyst depletion and regulate the local reaction environment [74,75]. In our case, a thin Nafion coating was sprayed onto the Ag/M catalyst layer (Fig. 4d), with an optimized Nafion content of 2% (Fig. S12c–f), resulting in the modified electrode denoted Ag/M@N. This electrode was then integrated into the microstructured membrane MEA (Ag/M@N_P).

When tested under identical electrolysis conditions, Ag/M@N_P exhibited stable and selective CO formation, achieving a FE_{CO} of 80% for 160 h at 400 mA cm^{-2} and an energy efficiency for CO (EE_{CO}) of 34%. This corresponds to more than a twofold increase in operational lifetime compared to the unmodified electrode. Post-electrolysis SEM/EDX characterization revealed a preserved catalyst layer morphology with only minor nanoparticle growth, yielding an average size of ~50 nm (Fig. S13a–c). Furthermore, EDX mapping and line scans confirmed strong N-species signals across the electrode surface (Fig. S13d,e), consistent with the retention of grafted melamine moieties. The primary role of the ionomer overlayer is to stabilize the melamine-functionalized interface by mitigating the loss of surface-bound species during operation. While ionomer layers can influence mass transport, control experiments (Fig. S12c–f) show that the ionomer alone does not provide a comparable stabilization effect in the absence of surface functionalization. Therefore, the improved durability arises from preserving the active interfacial chemistry rather than from the ionomer layer itself. The Nafion overlayer effectively retains the melamine species during extended operation, of over 160 h, highlighting the importance of stabilizing engineered interfacial structures in addition to optimizing intrinsic activity.

4. Conclusions

This study demonstrates that CO_2 availability in liquid-fed bicarbonate electrolysis is fundamentally governed by reaction–transport coupling at the membrane–electrode interface. Under high-current operation, effective performance depends not only on catalyst composition but on the regulation of multiphase CO_2 generation, retention, and transport within the interfacial region. By combining surface functionalization with interfacial morphology engineering, we modulate local CO_2 retention and gas–liquid distribution under convective flow conditions. Amine-functionalized catalyst layers improve interfacial CO_2 retention and buffer local acidity, while microstructured Nafion membranes alter multiphase transport by stabilizing localized gas-phase CO_2 holdup zones and mitigating interfacial depletion. Two-phase CFD analysis, coupled with electrochemical measurements, establishes a direct structure–transport–performance relationship, demonstrating that enhanced superficial CO_2 mass fraction and controlled phase distribution govern sustained activity. The integrated assemblies enable selective CO production with Faradaic efficiencies of ~80% at 500 mA cm^{-2} and stable operation exceeding 160 h. Long-term testing identifies interfacial modifier degradation as the primary durability constraint, which is effectively mitigated through a thin ionomer overlayer that preserves structural integrity under continuous operation. Overall, these results identify multiphase CO_2 transport and distribution as a critical engineering parameter in bicarbonate electrolysis and provide practical design guidance for scalable liquid-fed CO_2 conversion systems.

CRediT authorship contribution statement

Ilias Stamatelos: Writing – review & editing, Writing – original draft, Validation, Methodology, Investigation, Formal analysis, Data curation, Conceptualization. **Steffen Hess:** Software, Methodology, Investigation, Formal analysis, Data curation. **Joachim Pasel:** Writing – review & editing, Validation, Supervision, Funding acquisition. **Ralf Peters:** Writing – review & editing, Validation, Supervision, Resources.

Declaration of competing interest

The authors of this work have submitted provisional patents regarding the findings and the application potential of the electrolysis technology exhibited.

Acknowledgments

We are grateful to both H.H. Hardtdegen and M. Mikulics, who have performed the Raman studies in the optical lab of the Ernst Ruska Centre FZ Jülich (Prof. J. Mayer), and have also assisted us with their interpretation.

Appendix A. Supplementary data

Supplementary data to this article can be found online at https://doi.org/10.1016/j.cej.2026.176722.

Data availability

Data will be made available on request.

References

[1] R. Peters, N. Wegener, R.C. Samsun, F. Schorn, J. Riese, M. Grünewald, D. Stolten, Processes 10 (2022) 699.
[2] E.V. Kondratenko, G. Mul, J. Baltrusaitis, G.O. Larrazábal, J. Pérez-Ramírez, Energy Environ. Sci. 6 (2013) 3112–3135.
[3] O.S. Bushuyev, P. De Luna, C.T. Dinh, L. Tao, G. Saur, J. van de Lagemaat, S. O. Kelley, E.H. Sargent, Joule 2 (2018) 825–832.
[4] S. Nitopi, E. Bertheussen, S.B. Scott, X. Liu, A.K. Engstfeld, S. Horch, B. Seger, I.E. L. Stephens, K. Chan, C. Hahn, J.K. Nørskov, T.F. Jaramillo, I. Chorkendorff, Chem. Rev. 119 (2019) 7610–7672.
[5] X. Liu, J. Xiao, H. Peng, X. Hong, K. Chan, J.K. Nørskov, Nat. Commun. 8 (2017) 15438.
[6] J. Rosen, G.S. Hutchings, Q. Lu, S. Rivera, Y. Zhou, D.G. Vlachos, F. Jiao, ACS Catal. 5 (2015) 4293–4299.
[7] T. Zheng, K. Jiang, H. Wang, Adv. Mater. 30 (2018) 1802066.
[8] F. Liang, K. Zhang, L. Zhang, Y. Zhang, Y. Lei, X. Sun, Small 17 (2021) 2100323.
[9] R. Kortlever, J. Shen, K.J.P. Schouten, F. Calle-Vallejo, M.T.M. Koper, ACS Publications (2015).
[10] D.J. Wilhelm, D.R. Simbeck, A.D. Karp, R.L. Dickenson, Fuel Process. Technol. 71 (2001) 139–148.
[11] A.J. Welch, E. Dunn, J.S. DuChene, H.A. Atwater, ACS Energy Lett. 5 (2020) 940–945.
[12] J.A. Rabinowitz, M.W. Kanan, Nat. Commun. 11 (2020) 5231.
[13] J. Sisler, S. Khan, A.H. Ip, M.W. Schreiber, S.A. Jaffer, E.R. Bobicki, C.-T. Dinh, E. H. Sargent, ACS Energy Lett. 6 (2021) 997–1002.
[14] G. Lee, Y.C. Li, J.-Y. Kim, T. Peng, D.-H. Nam, A. Sedighian Rasouli, F. Li, M. Luo, A.H. Ip, Y.-C. Joo, E.H. Sargent, Nat. Energy 6 (2021) 46–53.
[15] Z. Zhang, E.W. Lees, S. Ren, B.A.W. Mowbray, A. Huang, C.P. Berlinguette, ACS Cent. Sci. 8 (2022) 749–755.
[16] M. Li, E. Irtem, H.-P. Iglesias van Montfort, M. Abdinejad, T. Burdyny, Nat. Commun. 13 (2022) 5398.
[17] T. Li, E.W. Lees, M. Goldman, D.A. Salvatore, D.M. Weekes, C.P. Berlinguette, Joule 3 (2019) 1487–1497.
[18] E.W. Lees, M. Goldman, A.G. Fink, D.J. Dvorak, D.A. Salvatore, Z. Zhang, N.W. X. Loo, C.P. Berlinguette, ACS Energy Lett. 5 (2020) 2165–2173.
[19] H. Song, C.A. Fernández, H. Choi, P.-W. Huang, J. Oh, M.C. Hatzell, Energy Environ. Sci. 17 (2024) 3570–3579.
[20] D.J.D. Pimlott, A. Jewlal, B.A.W. Mowbray, C.P. Berlinguette, ACS Energy Lett. 8 (2023) 1779–1784.
[21] Y. Rong, C. Yan, X. Li, J. Liu, X. Su, G. Zhang, D. Gao, G. Wang, X. Bao, Angew. Chem. Int. Ed. n/a (n.d.) e23118.
[22] B. Nourmohammadi Khiarak, G.T.S.T. da Silva, V. Grange, G. Gao, V. Golovanova, F.P. de García de Arquer, L.H. Mascaro, C.-T. Dinh, Small n/a (n.d.) 2409669.
[23] D. Wakerley, S. Lamaison, J. Wicks, A. Clemens, J. Feaster, D. Corral, S.A. Jaffer, A. Sarkar, M. Fontecave, E.B. Duoss, S. Baker, E.H. Sargent, T.F. Jaramillo, C. Hahn, Nat. Energy 7 (2022) 130–143.
[24] H. Ren, L. Zhu, H. Gu, Appl. Catal. B Environ. Energy 383 (2026) 126073.
[25] J.R. Pankhurst, P. Iyengar, A. Loiudice, M. Mensi, R. Buonsanti, Chem. Sci. 11 (2020) 9296–9302.
[26] G. Chamoulaud, D. Bélanger, J. Phys. Chem. C 111 (2007) 7501–7507.
[27] M. Zhao, L. Meng, L. Ma, G. Wu, Y. Wang, F. Xie, Y. Huang, RSC Adv. 6 (2016) 29654–29662.
[28] S. Kesavan, M.A. Raj, S.A. John, Anal. Biochem. 496 (2016) 14–24.
[29] J. Lyskawa, D. Bélanger, Chem. Mater. 18 (2006) 4755–4763.
[30] T. Yan, S. Liu, Z. Liu, J. Sun, P. Kang, Adv. Funct. Mater. 34 (2024) 2311733.
[31] L.-Y. Zhao, H. Wang, H. Tan, J. Chao, Z.-H. Lin, G.-C.-Q. Pan, X.-J. Wang, Q. Sun, Fuel 407 (2026) 137484.
[32] J. Hack, N. Maeda, D.M. Meier, ACS Omega 7 (2022) 39520–39530.
[33] G. Leverick, E.M. Bernhardt, A.I. Ismail, J.H. Law, A. Arifutzzaman, M.K. Aroua, B. M. Gallant, ACS Catal. 13 (2023) 12322–12337.
[34] I. Burgers, J. Jónasson, E. Goetheer, R. Kortlever, ChemSusChem n/a (n.d.) e202401631.
[35] K. Gao, Z. Gong, X. Chen, Y. Zhang, H. Chen, L. Jiang, C. Zhu, M. Ji, Y. Liu, Y. Cai, G. Li, G. Lu, ACS Appl. Mater. Interfaces 17 (2025) 33925–33934.
[36] H. Zhu, C. Zhang, N. Ma, M. Tao, W. Zhang, Appl. Catal. A Gen. 608 (2020) 117842.
[37] S. Santander, N. Padilla-Manzano, B. Díaz, R. Bacchiega, E. Jara, L.F. Álvarez, C. Pinto, J.C. Forero, P. Santana, E. Hamm, M. Urzúa, L. Tamayo, Pharmaceutics 15 (2023) 1659.
[38] P. Nazari, S. Zhao, O. Christensen, Z. Sun, M. Ceccato, J.V. Lauritsen, S. U. Pedersen, J. Rossmeisl, A. Rosas-Hernández, K. Daasbjerg, J. Am. Chem. Soc. 147 (34) (2025) 31395–31408.
[39] G. Lee, A.S. Rasouli, B.-H. Lee, J. Zhang, D.H. Won, Y.C. Xiao, J.P. Edwards, M. G. Lee, E.D. Jung, F. Arabyarmohammadi, H. Liu, I. Grigioni, J. Abed, T. Alkayyali, S. Liu, K. Xie, R.K. Miao, S. Park, R. Dorakhan, Y. Zhao, C.P. O'Brien, Z. Chen, D. Sinton, E. Sargent, Joule 7 (2023) 1277–1288.
[40] Y. Ke, W. Yuan, F. Zhou, W. Guo, J. Li, Z. Zhuang, X. Su, B. Lu, Y. Zhao, Y. Tang, Y. Chen, J. Song, Renew. Sust. Energy Rev. 145 (2021) 110860.
[41] S. Cuynet, A. Caillard, S. Kaya-Boussougou, T. Lecas, N. Semmar, J. Bigarré, P. Buvat, P. Brault, J. Power Sources 298 (2015) 299–308.
[42] H. Cho, S. Moon Kim, Y. Sik Kang, J. Kim, S. Jang, M. Kim, H. Park, J. Won Bang, S. Seo, K.-Y. Suh, Y.-E. Sung, M. Choi, Nat. Commun. 6 (2015) 8484.
[43] M. Lopez-Haro, L. Guétaz, T. Printemps, A. Morin, S. Escribano, P.-H. Jouneau, P. Bayle-Guillemaud, F. Chandezon, G. Gebel, Nat. Commun. 5 (2014) 5229.
[44] Q.K. Dang, D. Henkensmeier, N.N. Krishnan, J.H. Jang, H.-J. Kim, S.W. Nam, T.-H. Lim, J. Membr. Sci. 460 (2014) 199–205.
[45] S. Kang, G. Bae, S.-K. Kim, D.-H. Jung, Y.-G. Shul, D.-H. Peck, Int. J. Hydrog. Energy 43 (2018) 11386–11396.
[46] J. Sasahara, S. Cha, A. Chang-Chien, T. Kubota, N. Kuriyama, S.-J. Lee, Y. Liu, R. O'Hayre, F. Prinz, Y. Saito, Fuel Cell with Patterned Electrolyte/Electrode Interface US20020012825A1 (2002).
[47] A. Grondein, D. Bélanger, Carbon 50 (2012) 4335–4342.
[48] S. Kesavan, N.S.K. Gowthaman, S. Alwarappan, S.A. John, Sens. Actuators B 278 (2019) 46–54.
[49] M. Carmo, G.P. Keeley, D. Holtz, T. Grube, M. Robinius, M. Müller, D. Stolten, Int. J. Hydrog. Energy 44 (2019) 3450–3455.
[50] J. Greenwood, T.H. Phan, Y. Fujita, Z. Li, O. Ivasenko, W. Vanderlinden, H. Van Gorp, W. Frederickx, G. Lu, K. Tahara, Y. Tobe, H. Uji-i, S.F.L. Mertens, S. De Feyter, ACS Nano 9 (2015) 5520–5535.
[51] M. Mooste, E. Kibena-Põldsepp, M. Marandi, L. Matisen, V. Sammelselg, F. I. Podvorica, K. Tammeveski, J. Electroanal. Chem. 817 (2018) 89–100.
[52] X.T. Le, P. Viel, P. Jégou, A. Garcia, T. Berthelot, T.H. Bui, S. Palacin, J. Mater. Chem. 20 (2010) 3750–3757.
[53] T. Mikami, T. Yamamoto, M. Tomisaki, Y. Einaga, ACS Sustain. Chem. Eng. 10 (2022) 14685–14692.
[54] In: ResearchGate, n.d.
[55] X. Zeng, Y. Han, J. Yang, X. Li, Z. Lu, P. Cai, Z. Wen, J. Colloid Interface Sci. 701 (2026) 138757.
[56] C. Yan, Y.-J. Luo, W.-G. Zhang, Z.-F. Zhu, P.-Y. Li, N. Li, Y.-F. Chen, T. Jin, J. Appl. Polym. Sci. 139 (2022) 51992.
[57] D. Wang, Xiaoxian Zhang, S. Luo, S. Li, Adv. Mater. Phys. Chem. 2 (2013) 63–67.
[58] M. Zeiger, S. Fleischmann, B. Krüner, A. Tolosa, S. Bechtel, M. Baltes, A. Schreiber, R. Moroni, S. Vierrath, S. Thiele, V. Presser, RSC Adv. 6 (2016) 107163–107179.
[59] R. Pilot, R. Signorini, C. Durante, L. Orian, M. Bhamidipati, L. Fabris, Biosensors 9 (2019) 57.
[60] X. Huang, L. Xia, G. Li, Microchim. Acta 191 (2024) 758.
[61] A.C. Ferrari, J. Robertson, Phys. Rev. B 61 (2000) 14095–14107.
[62] A. Sadezky, H. Muckenhuber, H. Grothe, R. Niessner, U. Pöschl, Carbon 43 (2005) 1731–1742.
[63] M. Moskovits, J. Raman Spectrosc. 36 (2005) 485–496.
[64] A. Deryło-Marczewska, J. Goworek, S. Pikus, E. Kobylas, W. Zgrajka, Langmuir 18 (2002) 7538–7543.
[65] H. Farahmandazad, A. Grütter, S. Fu, R. Kortlever, E. Goetheer, W. de Jong, ACS Electrochem. 1 (10) (2025) 2106–2121.
[66] O. Gutiérrez-Sánchez, B. de Mot, N. Daems, M. Bulut, J. Vaes, D. Pant, T. Breugelmans, Energy Fuel 36 (2022) 13115–13123.
[67] I. Stamatelos, M. Rentzsch, C. Liu, F. Bauer, S. Barwe, M. Robert, ChemCatChem 16 (2024) e202300980.
[68] A. Raya-Imbernón, A.A. Samu, S. Barwe, G. Cusati, T. Fődi, B.M. Hepp, C. Janáky, ACS Energy Lett. 9 (2024) 288–297.
[69] G. Marcandalli, M.C.O. Monteiro, A. Goyal, M.T.M. Koper, Acc. Chem. Res. 55 (2022) 1900–1911.
[70] C.A. Obasanjo, G. Gao, J. Crane, V. Golovanova, F.P. García de Arquer, C.-T. Dinh, Nat. Commun. 14 (2023) 3176.
[71] R.B. Kutz, Q. Chen, H. Yang, S.D. Sajjad, Z. Liu, I.R. Masel, Energy Technol. 5 (2017) 929–936.
[72] C.-T. Dinh, F.P. García de Arquer, D. Sinton, E.H. Sargent, ACS Energy Lett. 3 (2018) 2835–2840.
[73] I. Stamatelos, C.-T. Dinh, W. Lehnert, M. Shviro, ACS Appl. Energy Mater. 5 (2022) 13928–13938.
[74] F.P.G. de Arquer, C.-T. Dinh, A. Ozden, J. Wicks, C. McCallum, A.R. Kirmani, D.-H. Nam, C. Gabardo, A. Seifitokaldani, X. Wang, Y.C. Li, F. Li, J. Edwards, L. J. Richter, S.J. Thorpe, D. Sinton, E.H. Sargent, Science 367 (2020) 661–666.
[75] A.P.L. Thévenot, T. Reiter, T. Ngo Thanh, L. Titze, C. Cazzaniga, F. Dionigi, P. Strasser, Energy Fuels 39 (2025) 8203–8210.